



Brightly Fluorescent Single-Walled Carbon Nanotubes via an Oxygen-Excluding Surfactant Organization

Sang-Yong Ju, *et al.*
Science **323**, 1319 (2009);
DOI: 10.1126/science.1166265

The following resources related to this article are available online at www.sciencemag.org (this information is current as of March 5, 2009):

Updated information and services, including high-resolution figures, can be found in the online version of this article at:

<http://www.sciencemag.org/cgi/content/full/323/5919/1319>

Supporting Online Material can be found at:

<http://www.sciencemag.org/cgi/content/full/323/5919/1319/DC1>

This article **cites 30 articles**, 6 of which can be accessed for free:

<http://www.sciencemag.org/cgi/content/full/323/5919/1319#otherarticles>

This article appears in the following **subject collections**:

Chemistry

<http://www.sciencemag.org/cgi/collection/chemistry>

Information about obtaining **reprints** of this article or about obtaining **permission to reproduce this article** in whole or in part can be found at:

<http://www.sciencemag.org/about/permissions.dtl>

22. C. H. Cho, F. St-Gelais, W. Zhang, S. Tomita, J. R. Howe, *Neuron* **55**, 890 (2007).
23. D. Soto, I. D. Coombs, L. Kelly, M. Farrant, S. G. Cull-Candy, *Nat. Neurosci.* **10**, 1260 (2007).
24. S. Tomita *et al.*, *Nature* **435**, 1052 (2005).
25. W. Vandenberghe, R. A. Nicoll, D. S. Bredt, *Proc. Natl. Acad. Sci. U.S.A.* **102**, 485 (2005).
26. C. Bats, L. Groc, D. Choquet, *Neuron* **53**, 719 (2007).
27. L. Chen *et al.*, *Nature* **408**, 936 (2000).
28. K. Menuz, G. A. Kerchner, J. L. O'Brien, R. A. Nicoll, *Neuropharmacology* **56**, 22 (2009).
29. K. Menuz, J. L. O'Brien, S. Karmizadegan, D. S. Bredt, R. A. Nicoll, *J. Neurosci.* **28**, 8740 (2008).
30. M. Fukaya, M. Yamazaki, K. Sakimura, M. Watanabe, *Neurosci. Res.* **53**, 376 (2005).
31. N. Klugbauer *et al.*, *FEBS Lett.* **470**, 189 (2000).
32. H. Berkefeld *et al.*, *Science* **314**, 615 (2006).
33. J. Liu, J. Xia, K. H. Cho, D. E. Clapham, D. Ren, *J. Biol. Chem.* **282**, 18945 (2007).
34. M. S. Nadal *et al.*, *Neuron* **37**, 449 (2003).
35. U. Schulte *et al.*, *Neuron* **49**, 697 (2006).
36. Materials and methods are available as supporting material on Science Online.
37. C. Bokel, S. Dass, M. Wilsch-Brauninger, S. Roth, *Development* **133**, 459 (2006).
38. H. Hoshino *et al.*, *Mol. Biol. Cell* **18**, 1143 (2007).
39. S. Roth, F. S. Neuman-Silberberg, G. Barcelo, T. Schupbach, *Cell* **81**, 967 (1995).
40. L. Chen, S. Bao, X. Qiao, R. F. Thompson, *Proc. Natl. Acad. Sci. U.S.A.* **96**, 12132 (1999).
41. K. Hashimoto *et al.*, *J. Neurosci.* **19**, 6027 (1999).
42. B. Hille, *Ion Channels of Excitable Membranes* (Sinauer Associates, Sunderland, MA, ed. 3, 2001).
43. D. Turetsky, E. Garringer, D. K. Patneau, *J. Neurosci.* **25**, 7438 (2005).
44. C. Antz *et al.*, *Nat. Struct. Biol.* **6**, 146 (1999).
45. D. S. Koh, J. R. Geiger, P. Jonas, B. Sakmann, *J. Physiol.* **485**, 383 (1995).
46. D. Colquhoun, P. Jonas, B. Sakmann, *J. Physiol.* **458**, 261 (1992).
47. C. P. Castro, D. Piscopo, T. Nakagawa, R. Derynck, *J. Cell Sci.* **120**, 2454 (2007).
48. Y. Sun *et al.*, *Nature* **417**, 245 (2002).
49. B. Barbour, M. Häusser, *Trends Neurosci.* **20**, 377 (1997).
50. A. Rollenhagen *et al.*, *J. Neurosci.* **27**, 10434 (2007).
51. We thank J. P. Adelman for insightful comments and critical reading of the manuscript and A. Haupt for help with bioinformatics. This work was supported by grants of the Deutsche Forschungsgemeinschaft to B.F. (SFB 746/TP16, SFB780/TPA3, EXC 294) and to N.K. (SFB780/TPB4).

Supporting Online Material

www.sciencemag.org/cgi/content/full/323/5919/1313/DC1
Materials and Methods
Figs. S1 to S6
Table S1
References

29 October 2008; accepted 16 January 2009
10.1126/science.1167852

REPORTS

Brightly Fluorescent Single-Walled Carbon Nanotubes via an Oxygen-Excluding Surfactant Organization

Sang-Yong Ju,¹ William P. Kopcha,² Fotios Papadimitrakopoulos^{1,2*}

Attaining high photoluminescence quantum yields for single-walled carbon nanotubes (SWNTs) in order to broaden their optoelectronics and sensing applications has been a challenging task. Among various nonradiative pathways, sidewall chemisorption of oxygen provides a known defect for exciton quenching through nanotube hole doping. We found that an aliphatic (dodecyl) analog of flavin mononucleotide, FC12, leads to high dispersion of SWNTs, which tend to aggregate into bundles. Unlike other surfactants, the surface organization of FC12 is sufficiently tight to exclude oxygen from the SWNT surface, which led to quantum yields as high as 20%. Toluene-dispersed, FC12-wrapped nanotubes exhibited an absorption spectrum with ultrasharp peaks (widths of 12 to 25 milli-electron volts) devoid of the characteristic background absorption of most nanotube dispersions.

The ability to readily assign the (*n,m*) chirality of semiconducting single-walled carbon nanotubes (SWNTs) by means of photoluminescence excitation (PLE) mapping (1), together with their photostability (2), holds promise for applications in optoelectronics (3), biological imaging (2, 4), and sensing (4). Although the optical properties of SWNTs are excitonic in nature (5), these structures exhibit low-fluorescence quantum yields. Possible causes include low-lying, nonradiative states (dark excitons) (6) or various defects that, as a result of the large exciton diffusion length (~90 nm) in SWNTs, contribute to substantial photoluminescence quenching (7, 8). Oxygen in particular, in

the presence of an acid or neutral environment (9), can quench photoluminescence through hole doping and subsequent nonradiative Auger recombination (8, 10).

To make matters worse, nanotube bundling (11, 12), along with chemical defects resulting from covalent functionalization (13) and nanotube inhomogeneities (14), can further decrease or completely quench nanotube luminescence. Individual SWNTs can have photoluminescence quantum yields as high as 8% (15), but solution-suspended SWNTs have shown much lower quantum yields [i.e., 1.5% for polyfluorene (PFO)-wrapped SWNTs (16), 1.1% for purified DNA-wrapped SWNTs (11), and less than 0.1% for surfactant-micellarized nanotubes (16, 17)]. Most SWNT surfactants allow oxygen to interact and dope these nanotubes, and are sufficiently labile that they allow the nanotubes to reform bundles (9). Here, we show that a low-molecular-weight, organic-soluble analog of flavin mono-

nucleotide, FC12, imparts considerable individualization in toluene and other aromatic solvents (i.e., *o*-xylene and benzene). In addition, the tight self-organization of FC12 around SWNTs leads to an effective exclusion of oxygen that affords quantum yields as high as 20%.

Flavin mononucleotide (FMN), a common redox cofactor related to vitamin B₂, was recently shown to self-organize around SWNTs through a helical conformation (18). Such helical wrapping (Fig. 1, A and B) originates from two sets of self-recognizing H-bonds that "stitch" the neighboring FMN moieties into a continuous helical ribbon (Fig. 1A), the concentric π - π interaction of the isoalloxazine ring with the underlying graphene sidewalls (Fig. 1B), and a soluble *d*-ribose phosphate side group that imparts effective solubilization in aqueous media. In an effort to broaden flavin-based dispersion in organic solvents, we synthesized an isoalloxazine derivative with an aliphatic (dodecyl) side group, termed FC12. The synthetic route of FC12 involves two facile steps with an overall yield of ~35% (19). FC12 dispersions of CoMoCAT (Co-Mo bimetallic catalyst synthesized) SWNTs (20) were obtained by sonicating 1 mg of FC12, 1 mg of SWNTs, and 4 ml of various solvents for 4 hours at 300 W. The mixture was centrifuged for 20 min at 10,000g, which eliminated visible SWNT bundles in various solvents [i.e., benzene, toluene, *o*-xylene, ethylacetate, tetrahydrofuran (THF), pyridine, acetone, and *N,N*-dimethyl formamide (DMF)]. Table 1 summarizes the physical properties of these solvents as a function of dielectric constant (ϵ). SWNT photoluminescence was observed for only some of these solvents: benzene, toluene, *o*-xylene, ethylacetate, THF, and acetone (see below).

PLE maps for benzene, toluene, ethylacetate, and acetone show that the photoluminescence intensity (~315,000 counts) of FC12-(6,5)-SWNTs in toluene dispersion is 15 to 20 times

¹Nanomaterials Optoelectronics Laboratory, Polymer Program, University of Connecticut, Storrs, CT 06269, USA.
²Department of Chemistry, Institute of Materials Science, University of Connecticut, Storrs, CT 06269, USA.

*To whom correspondence should be addressed. E-mail: papadim@mail.ims.uconn.edu

that for other solvents (see maximum intensity in the bottom of each panel in Fig. 2; table S1 lists the relative photoluminescence intensities as a function of nanotube species, diameter, and chiral angle). In all PLE maps, all intensity maxima from the observed first (E_{11}^S) and second (E_{22}^S) electronic transitions of semiconducting SWNTs are similarly redshifted as in the case of FMN (18). The similar E_{11}^S and E_{22}^S redshift trend in organic solvents, as in the case of FMN in H₂O (i.e., 15 to 51 nm for E_{11}^S and 23 to 71 nm for E_{22}^S), is in agreement with the tight organization of flavin around SWNTs (18). Figure S2 plots the relative photoluminescence intensity of Fig. 2, B to D, as a function of nanotube diameter d_t . With the exception of (7,5)-SWNTs, which are more abundant in toluene, the relative photoluminescence intensities of the observed nanotube species do not change appreciably with d_t . However, the average photoluminescence full width at half-maximum (FWHM) values of all nanotube species in the solvents with low dielectric constant (i.e., 26 and 27 meV for benzene and toluene, respectively) are significantly less than those in the high-dielectric solvents (i.e., 39 and 45 meV for ethylacetate and acetone, respectively) (table S1). The larger FWHM and lower photoluminescence intensities indicate either large inhomogeneity in FC12 functionalization, or a greater degree of bundling than in the benzene and toluene dispersions, or both.

Tan *et al.* (12) reported that SWNT aggregation enhances exciton energy transfer (EET) between SWNTs within bundles, where excitation of large band gap tubes leads to emission from SWNTs with smaller band gaps. Such spectral features are easily discernible for species with high concentrations, as in the case of (6,5) and (7,5) for CoMoCAT SWNTs (20). The red arrows in Fig. 2, A to D, indicate such an EET feature between (6,5)- and (7,5)-SWNTs. When normalized to the PLE intensity of (7,5)-SWNTs, the (6,5) \rightarrow (7,5) EET feature from the benzene and toluene is smaller than those seen in ethylacetate and acetone by a factor of 2 to 3 (fig. S3). This result provides an initial indication that SWNT individualization in toluene is one of the

reasons for the higher photoluminescence intensity and narrower peaks.

Figure 3A illustrates the corresponding visible–near infrared (Vis–NIR) spectra of FC12-dispersed SWNTs in acetone, ethylacetate, and toluene. The toluene absorption spectrum shows sharper peaks that are shifted to higher energies with respect to those of ethylacetate and acetone, as well as a nearly flat baseline. Note that the three absorption curves in Fig. 3A are not offset with

respect to each other; rather, they reside on a power-law background ($a\lambda^{-b}$, where λ is the wavelength and a and b are fitted parameters) (19, 21). In addition, the E_{11}^S/E_{22}^S ratio of (6,5)-SWNTs, ~ 6 , is the highest reported thus far, with DNA-wrapped (22), PFO-wrapped (16), and sodium dodecyl benzene sulfonate (SDBS)-dispersed (23) SWNTs showing E_{11}^S/E_{22}^S ratios of 3, 3.5, and 3.5, respectively for (6,5)- or (7,5)-SWNTs. Moreover, the (6,5) E_{11}^S/E_{22}^S ratio is ~ 6

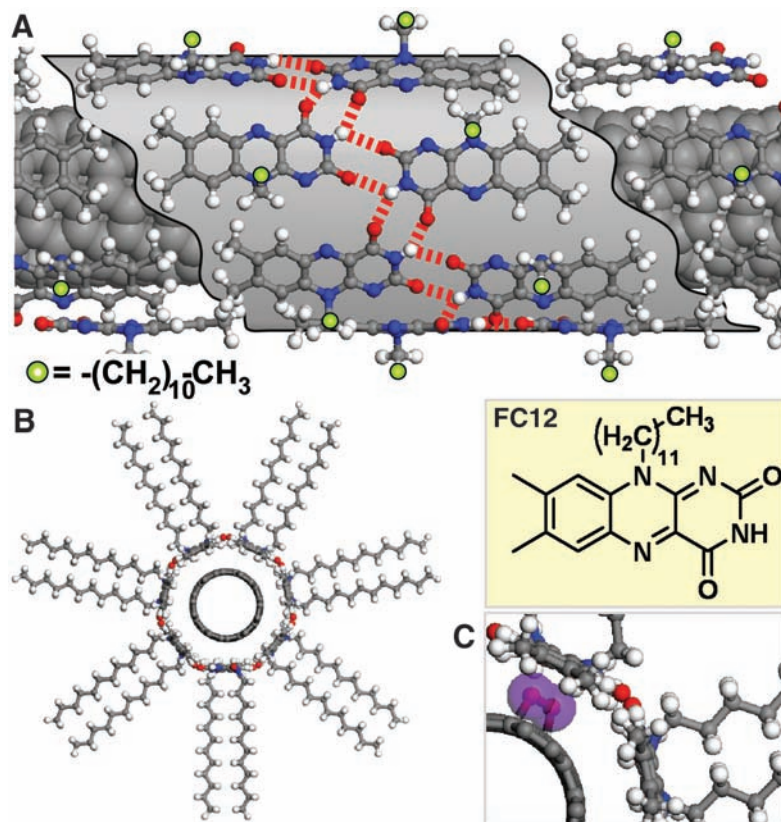


Fig. 1. (A) Top view of isoalloxazine moieties of FC12 wrapped in a 7_1 helical pattern. Red dotted lines and green spheres depict the intermolecular H-bonding between neighboring isoalloxazine moieties and the positions of the solubilizing side chains (undecyl), respectively. Color code for atoms: gray, carbon; white, hydrogen; blue, nitrogen; red, oxygen. (B) Side view illustrates the tight 7_1 helical wrapping of FC12 around (6,5)-SWNTs, which greatly interferes with the presence of a chemisorbed oxygen species (i.e., 1,4-endoperoxide and its van der Waals radii illustrated in purple) (C).

Table 1. Quantum yield values for (6,5)-SWNTs as a function of solvent dielectric constant (ϵ), H-bonding nature, and solubility values for FC12 and lumiflavin.

Solvent	Photoluminescence activity	Quantum yield of (6,5)-SWNTs (%)		ϵ	H-bonding capability*	Lumiflavin solubility ($\mu\text{g/ml}$)	FC12 solubility (mg/ml)	Max. E_{11}^S absorption
		"Sample"	"Individual"					
Benzene	Yes	5	10	2.3	P	4.4	0.31	0.01
Toluene	Yes	11	20	2.4	P	4.3	0.23	0.03
<i>o</i> -Xylene	Yes	8.7	16.9	2.5	P	5.9	0.25	0.02
Ethylacetate	Yes	0.024	0.4	6	M	14.1	0.51	0.075
THF	Yes	0.07	0.1	7	M	46.2	11.03	0.21
Pyridine	No	—	—	12.5	M-S	528.7	70.38	0.3
Acetone	Yes	0.08	0.2	21	M	53.9	1.81	0.14
DMF	No	—	—	39	M-S	316.7	22.87	0.7
D ₂ O†	Yes	0.08	0.8	79	S	—	—	0.19

*P, poor; M, moderate; M-S, moderate-strong (32). †FMN-dispersed SWNTs in D₂O.

only for toluene, dropping to ~ 3.5 and 4 for ethylacetate and acetone FC12 dispersions, respectively. Because the E_{11}^S transitions are more susceptible to doping-induced bleaching than are the E_{22}^S transitions (9), larger E_{11}^S/E_{22}^S ratios are indicative of a more pristine nature for the SWNTs.

A close-up of the toluene E_{11}^S spectral range, along with peak deconvolution based on the

PLE-observed SWNTs, is shown in Fig. 3B. The background-subtracted absorption spectrum (circles) was deconvoluted with a multiplicity of Lorentzian peaks, where their maxima were allowed to vary 1 to 2 nm from the corresponding PLE-derived position (table S1) along with unrestricted FWHM (19). The NIR spectra were adequately described by a simple summation of the individual (n,m) -SWNTs observed in the

corresponding PLE map of Fig. 2B. This one-to-one correlation between photoluminescence and absorption spectra indicates profound individualization for all observed nanotubes. With the exception of (7,6)-SWNTs, whose FWHM coincides with H₂O absorption, the FWHM values of all nanotubes range from 12 to 25 meV, with an average of 18 meV (22 meV for weighted average) (table S2). Comparison of these results with previously reported FWHM absorption values for DNA-wrapped nanotubes (18 to 24 meV) (22) and PFO-dispersed nanotubes (19 to 20 meV) (16) provides additional support for the idea that the helical wrapping of FC12 affords a highly uniform environment around these SWNTs (24).

To assess the deconvolution fidelity of Fig. 3B, we compared the percent abundance obtained by absorbance (Fig. 3B) and PLE intensities (table S2). The diameter (d_i), modality [$\text{mod}(n-m,3) = 1$ or 2], family ($2n+m = \text{constant}$), and (n,m) chirality of SWNTs all influence their absorptivity and corresponding photoluminescence efficiency (25, 26). Our group (21), as well as others (15, 27), have indicated that the theoretically calculated absorption [$J_{\text{cal}}^{\text{abs}}(n,m)$] and photoluminescence [$J_{\text{cal}}^{\text{PL}}(n,m)$] intensity factors calculated by Oyama *et al.* (25) provide a good framework for correlating (n,m) abundance between absorbance and photoluminescence results. Columns 4 and 5 of table S2 list the experimentally observed relative (n,m) -SWNT abundance as obtained by absorbance and PLE results, respectively. When these results are scaled by the Oyama-derived factors (columns 7 and 8), the average divergence between the absorbance- and photoluminescence-derived abundance results (0.12) becomes less than the divergence of the unscaled abundances (0.18).

What is the nature of the significantly greater background absorption for ethylacetate and

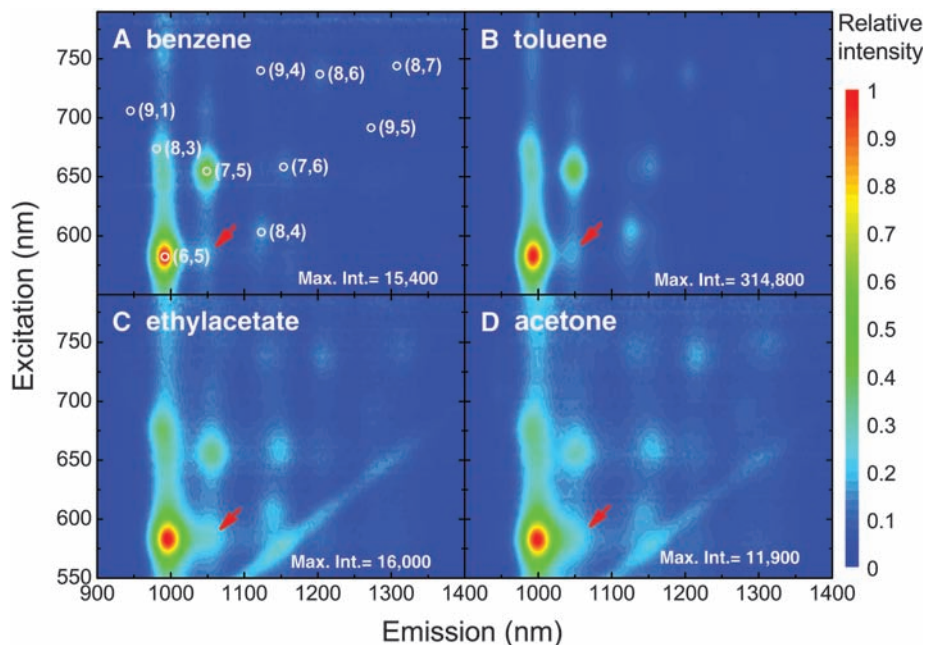
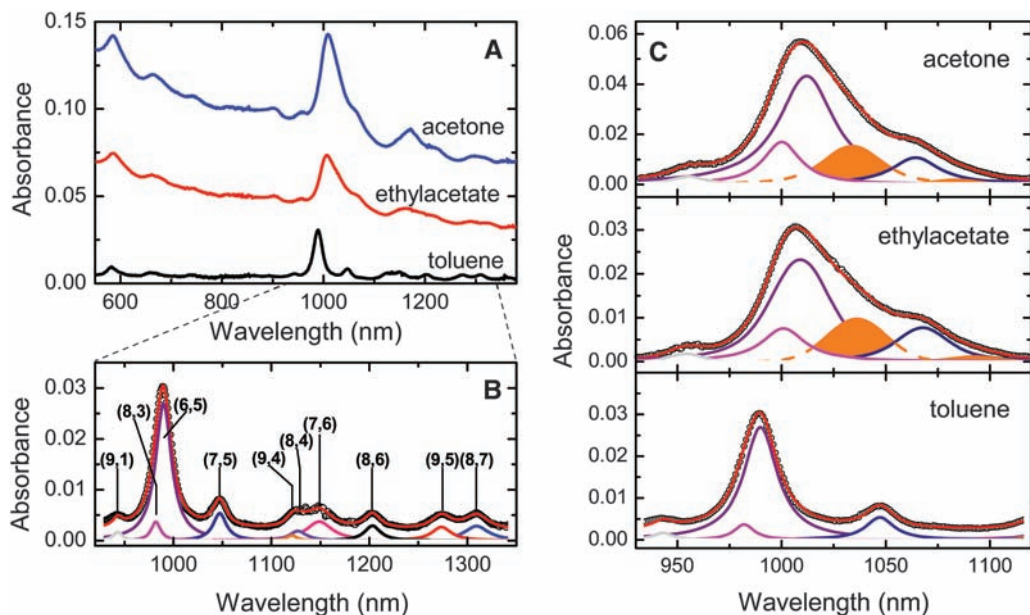


Fig. 2. Solvent-driven influences on the photoluminescence characteristics and brightness (maximum intensity counts) of FC12-dispersed CoMoCAT SWNTs. Numbers in parentheses and white circles indicate the (n,m) chiral indices and peak position, respectively, of various SWNT species in (A) benzene, (B) toluene, (C) ethylacetate, and (D) acetone. The toluene FC12-SWNT dispersion shows a maximum photoluminescence intensity (314,800 counts) for a significantly lesser amount of SWNTs according to Fig. 3A. Red arrows depict EET features from large to small band gap nanotubes.

Fig. 3. Aggregation-induced spectral purity of FC12-dispersed SWNTs, as deduced by spectral deconvolution of their electronic absorption in various solvents. (A) Nonoffset Vis-NIR absorption spectra of FC12-dispersed SWNTs in acetone, ethylacetate, and toluene. (B) Deconvoluted NIR region of the toluene sample, based on the PLE-observed (n,m) -SWNT species of Fig. 2B. Circles and red curves denote the experimental and reconstructed spectra from the summation of the color-coded Lorentzian peaks, assigned to various (n,m) nanotubes. The former curves were offset upward by 0.002 absorbance units to facilitate visual comparison. (C) Absorption spectra from acetone, ethylacetate, and toluene FC12-SWNT dispersions from 930 to 1120 nm, along with their deconvoluted components depicting the color-coded (9,1)-, (8,3)-, (6,5)-, and (7,5)-SWNT species, in conjunction with two orange-colored Gaussians attributed to aggregate absorptions from the major (6,5) and (7,5) nanotube species.



acetone? Figure 3C illustrates the deconvoluted window from 930 to 1120 nm of Fig. 3A. This region contains the E_{11}^S absorptions of the most abundant (6,5)- and (7,5)-SWNTs in CoMoCAT sample (20), along with (9,1)- and (8,3)-SWNTs. After background subtraction (19), the pronounced features of (9,1)-, (6,5)-, and (7,5)-SWNTs allowed us to determine an average redshift of 21 meV for all three absorptions. When we redshifted and confined the peak position of all four nanotube absorptions of Fig. 3A and allowed peak height and FWHM optimization for Fig. 3C, the resulting fits (for several attempts) reproduced poorly the 1025 to 1050 nm and the 1075- to 1100-nm regions of ethylacetate and acetone sample, which are not occupied by any nanotubes (fig. S4). To account for this shortcoming, we introduced two Gaussian peaks in these positions (highlighted in orange), and re-deconvoluted these spectra, to obtain an optimum fit. These two Gaussian peaks are shifted by an average of ~ 27 meV compared to the redshifted positions of (6,5) and (7,5)-SWNTs. Substitution of these two Gaussian peaks with Lorentzian shape produced a less optimum fit, indicative of an ensemble rather than an individual nanotube species.

Dynamic light scattering (DLS) was used to qualitatively assess the presence or absence of nanotube bundling in various solvents. In order to minimize laser absorption by both nanotube and the tail-end of FC12 that inadvertently interferes with size-dependent Brownian motion through thermal convection, we used a 633 nm laser line at 5 mW intensity power. Badaire *et al.* (28) reported that for laser powers below 150 mW, SWNT-related thermal convection effects become insignificant. The time-dependent auto-correlation function, $C(t)$, for the toluene and ethylacetate dispersed FC12-SWNT samples of Fig. 3A, are shown in fig. S5. After the rapid initial $C(t)$ decay, the toluene dispersion exhibits only a minor fluctuation between 20 and 75 μ s. However, the ethylacetate dispersion exhibits a broad fluctuation spanning in excess of 400 μ s, indicative of large bundling (28).

The presence of small and large SWNT bundles has been previously observed (11, 12, 29). Density gradient centrifugation has been used to fractionate, according to buoyancy, surfactant-suspended SWNTs in bundles of different diameter (11). Small bundles were shown to exhibit a progressively redshifted absorption (as high as 19 meV) and larger FWHM relative to individualized SWNTs. Similarly, their photoluminescence emissions were broader, were redshifted, and had considerably smaller photoluminescence quantum yields. These findings are in good agreement with the 21 meV in average redshift of the main E_{11}^S absorptions in Fig. 3C. This, along with the broader FWHM in both PLE and absorption spectra of ethylacetate and acetone FC12 dispersions, indicates that bundling is a major factor in luminescence quenching.

The profoundly intense PLE signal of toluene-dispersed FC12 dispersion, in particular that of the (6,5)-SWNTs, prompted us to determine their photoluminescence quantum yield using the method in (11). The absorbance (Fig. 4A) and emission (Fig. 4B) spectra of Styryl-13 were compared with the E_{22}^S absorption and E_{11}^S emission profiles of SDS- and FC12-dispersed CoMoCAT SWNTs. The 11% quantum yield of Styryl-13 at 3.3×10^{-7} M in methanol was used as a primary reference standard because of the close excitation and emission spectral overlap with (6,5)-SWNTs (11). Before determining the quantum yield of toluene-dispersed FC12-SWNTs, we used the aqueous-dispersed SDS-SWNTs as a secondary standard (16, 17). Because the power-law background signal in both SDS and FC12 can influence significantly the nanotube quantum yield figures, we define as “sample” and “individual” quantum yields the values obtained when (6,5) absorption is taken from either zero absorbance units or the power-law fitted line, respectively. Figure S6 illustrates sample quantum yields of SDS-dispersed (6,5)-SWNTs as a function of their E_{22}^S absorption peak intensity. A value of 0.5% for the “sample” quantum yield was obtained at ultimate dilution while keeping the SDS concentration above the critical micelle concentration of ~ 1 weight percent (16, 17). Progressively higher concentrations decrease the quantum yield down to 0.05% and below, in accordance with (16, 17). The substantially higher photoluminescence intensity of FC12- versus SDS-dispersed SWNTs (Fig. 4B) yields a “sample” quantum yield of $\sim 11\%$ for (6,5)-SWNTs. When the scattering background is removed, the “individual” (6,5) quantum yield increases to $\sim 20\%$. Table 1 lists the corresponding (6,5) quantum yields for all solvents in this study. *o*-Xylene and

benzene demonstrated 17% and 10% “individual” quantum yield for (6,5)-SWNTs, respectively, with the remaining solvents showing progressively lower quantum yield values.

There may be several causes for the surprisingly large quantum yields for (6,5)-SWNTs. Near-armchair nanotubes such as (6,5)-SWNTs have been theorized to exhibit progressively higher quantum yields as their diameter decreases (25, 30), although modality and family dependence also play an important role. Such increases, however, together with recent $\sim 8\%$ quantum yield determination for SDBS-suspended SWNTs (using single-nanotube photometry) (15), cannot explain the aforementioned 20% quantum yield value for (6,5)-SWNTs. Similarly, the possibility of selective enrichment of only (6,5)-SWNTs can easily be ruled out on the basis of one-to-one correlation between photoluminescence and NIR absorption, as well as the close resemblance of the relative photoluminescence abundance histograms for FC12- and SDS-dispersed nanotubes in fig. S2.

To pinpoint the nature of such a high quantum yield, we investigated the tight wrapping of FC12 onto nanotubes by time-dependent photoluminescence intensity traces as a function of O_2 . Unlike SDS dispersion, which exhibits progressively lower photoluminescence as a function of irradiation (9), the photoluminescence intensity of toluene FC12 dispersion remained constant (Fig. 4C). Although the reversible acid-induced p-doping of SWNTs in the presence of oxygen is well documented (7–9), less attention has been exerted on SWNT interactions with oxygen alone (8). Density functional theory calculations by Dukovic *et al.* (8) indicate that singlet O_2 chemisorbs on a (5,0)-SWNT and adopts a 1,4-endoperoxide structure (Fig. 1C). The calculated activation energy for 1,4-endoperoxide desorp-

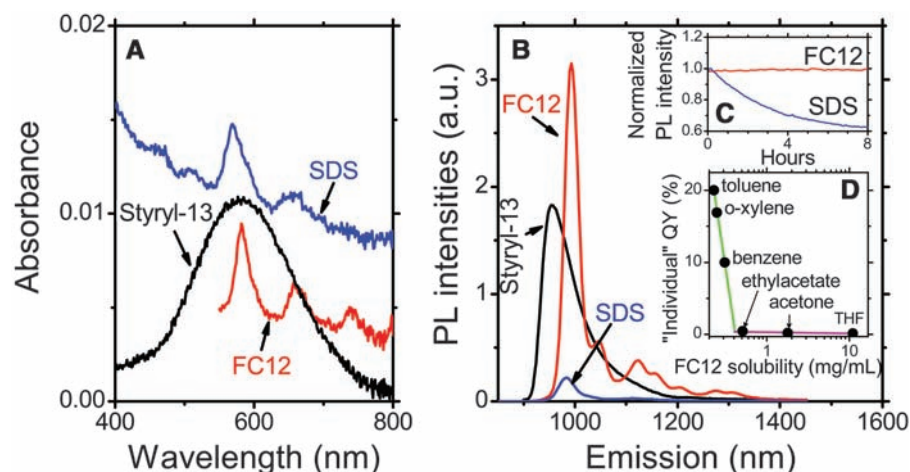


Fig. 4. Quantum yield determination and photo-oxidation stability of SDS- and FC12-dispersed SWNTs. Quantum yield values for (6,5)-SWNTs were determined by comparing their electronic absorption (A) and photoluminescence emission (B) relative to a Styryl-13 reference standard (11). (C) Normalized photoluminescence intensity behavior of (6,5)-SWNTs as a function of irradiation time in their respective D_2O and toluene media. (D) “Individual” quantum yield dependence of (6,5)-SWNTs versus FC12 solubility in various solvents.

tion (~ 1 eV) (8) is about half of the binding energy of a single isoalloxazine moiety (~ 2.2 eV) (31), which suggests that chemisorbed O_2 should be displaced by FC12 organization around the nanotubes. As illustrated in Fig. 1C, the seamless isoalloxazine wrapping is severely prohibited in the presence of a chemisorbed 1,4-endoperoxide because of van der Waals repulsions. In contrast to FC12, the loose organization of other surfactants (such as SDS and SDBS) around SWNTs permits the inclusion of these 1,4-endoperoxide defects. We note that PFO-wrapped SWNTs, in which the surfactant is more organized, have a greater nanotube “sample” photoluminescence quantum yield (1.5%) (16) versus 0.1 to 0.5% for SDS-dispersed SWNTs (16, 17).

The origin of the large solvent variation in the observed photoluminescence quantum yield may originate in the relative solubility differences of the two FC12 submoieties (i.e., isoalloxazine ring and dodecyl side chain). We procured 10-methyl isoalloxazine (lumiflavin), the closest analog to the isoalloxazine ring, and investigated its solubility characteristics versus those of FC12. Table 1 lists the solubilities of lumiflavin and FC12 as a function of dielectric constant (ϵ) of various solvents. Both lumiflavin and FC12 exhibit significantly reduced solubilities in nonpolar solvents (i.e., benzene, toluene, and *o*-xylene), with toluene the lowest. As solvent polarity increases (i.e., ethylacetate, THF, and acetone), their solubilities increase accordingly. Pyridine and DMF exhibit the highest solubility values for both lumiflavin and FC12, although SWNT photoluminescence activity is absent. Such behavior would originate from the moderate to strong H-bonding ability of pyridine and DMF, which would dissociate the H-bonded FC12 ribbon responsible for nanotube dispersion.

The “individual” quantum yield of (6,5)-SWNTs is shown in Fig. 4D as a function of FC12 solubility in each solvent (Table 1). High quantum yields (green line) were seen for low-polarity solvents, and low quantum yields (magenta line) were seen for medium-polarity solvents. For both regimes, the increase in FC12 solubility was followed by a decrease in quantum yield. Because H-bonding is responsible for both helix stability and FC12 (or lumiflavin) dissolution, increasing solvent polarity is expected to increase the helix dissociation constant and render FC12-wrapped nanotubes more prone to bundling and less able to desorb 1,4-endoperoxide defects. The proportionality of the helix dissociation constant to the FC12 solubility would account for the linear dependence of 1,4-endoperoxide defect removal along the one-dimensional SWNT structure. The uniform and defect-free environment offered by the flavin organization, which is needed as a result of the large exciton diffusion length (~ 90 nm) (7) in SWNTs, opens an array of new frontiers in SWNT photophysics. Moreover, the flavin organization is also compliant with the hierarchical assembly of nanotubes for device manipulation.

References and Notes

1. S. M. Bachilo *et al.*, *Science* **298**, 2361 (2002); published online 29 November 2002 (10.1126/science.1078727).
2. D. A. Heller, S. Baik, T. E. Eurell, M. J. Strano, *Adv. Mater.* **17**, 2793 (2005).
3. J. Chen *et al.*, *Science* **310**, 1171 (2005).
4. P. W. Barone, S. Baik, D. A. Heller, M. S. Strano, *Nat. Mater.* **4**, 86 (2005).
5. F. Wang, G. Dukovic, L. E. Brus, T. F. Heinz, *Science* **308**, 838 (2005).
6. V. Perebeinos, J. Tersoff, P. Avouris, *Nano Lett.* **5**, 2495 (2005).
7. L. Cognet *et al.*, *Science* **316**, 1465 (2007).
8. G. Dukovic *et al.*, *J. Am. Chem. Soc.* **126**, 15269 (2004).
9. M. S. Strano *et al.*, *J. Phys. Chem. B* **107**, 6979 (2003).
10. F. Wang, G. Dukovic, E. Knoesel, L. E. Brus, T. F. Heinz, *Phys. Rev. B* **70**, 241403 (2004).
11. J. Crochet, M. Clemens, T. Hertel, *J. Am. Chem. Soc.* **129**, 8058 (2007).
12. P. H. Tan *et al.*, *Phys. Rev. Lett.* **99**, 137402 (2007).
13. M. S. Strano *et al.*, *Science* **301**, 1519 (2003).
14. Y. Miyamoto, A. Rubio, S. Berber, M. Yoon, D. Tomanek, *Phys. Rev. B* **69**, 121413 (2004).
15. D. A. Tsybolski, J. D. R. Rocha, S. M. Bachilo, L. Cognet, R. B. Weisman, *Nano Lett.* **7**, 3080 (2007).
16. A. Nish, J.-Y. Hwang, J. Doig, R. J. Nicholas, *Nat. Nanotechnol.* **2**, 640 (2007).
17. M. J. O'Connell *et al.*, *Science* **297**, 593 (2002).
18. S.-Y. Ju, J. Doll, I. Sharma, F. Papadimitrakopoulos, *Nat. Nanotechnol.* **3**, 356 (2008).
19. See supporting material on Science Online.
20. S. M. Bachilo *et al.*, *J. Am. Chem. Soc.* **125**, 11186 (2003).
21. Z. Luo, L. D. Pfefferle, G. L. Haller, F. Papadimitrakopoulos, *J. Am. Chem. Soc.* **128**, 15511 (2006).
22. M. Zheng, E. D. Semke, *J. Am. Chem. Soc.* **129**, 6084 (2007).
23. Y. Tan, D. E. Resasco, *J. Phys. Chem. B* **109**, 14454 (2005).
24. O. Kiowski *et al.*, *Phys. Rev. B* **75**, 075421 (2007).
25. Y. Oyama *et al.*, *Carbon* **44**, 873 (2006).
26. C. Fantini *et al.*, *Phys. Rev. Lett.* **93**, 147406 (2004).
27. B. Wang *et al.*, *J. Am. Chem. Soc.* **129**, 9014 (2007).
28. S. Badaire, P. Poulin, M. Maugey, C. Zakri, *Langmuir* **20**, 10367 (2004).
29. A. Hagen, T. Hertel, *Nano Lett.* **3**, 383 (2003).
30. S. Reich, C. Thomsen, J. Robertson, *Phys. Rev. Lett.* **95**, 077402 (2005).
31. C. S. Lin, R. Q. Zhang, T. A. Niehaus, T. Frauenheim, *J. Phys. Chem. C* **111**, 4069 (2007).
32. D. W. V. Krevelen, *Properties of Polymers* (Elsevier, New York, ed. 3, 1990).
33. We thank S. Vaddiraju, J. Doll, D. Abanulo, A. Nish, and R. J. Nicholas for useful discussions. Supported mainly by Air Force Office of Scientific Research grant FA9550-06-1-0030, and in part by NSF grants NIRT DMI-0422724 and CBET-0828771/0828824 and NIH grant ES013557.

Supporting Online Material

www.sciencemag.org/cgi/content/full/323/5919/1319/DC1
Materials and Methods

Figs. S1 to S6

Tables S1 and S2

References

23 September 2008; accepted 21 January 2009
10.1126/science.1166265

Probing the Angular Momentum Character of the Valence Orbitals of Free Sodium Nanoclusters

C. Bartels, C. Hock, J. Huwer,* R. Kuhnen, J. Schwöbel,† B. von Issendorff‡

Although many properties of polyatomic metal clusters have been rationalized by an electron shell model resembling that used for free atoms, it remained unclear how reliable this analogy is with respect to the angular momentum eigenstate character of the electronic wave functions. We studied free size-selected negatively charged clusters of sodium atoms (Na_n^-) of approximately spherical shape ($n = 19, 40, 55, 58, 147$) by angle-resolved photoelectron spectroscopy over a broad range of photon energies (1.5 to 5 electron volts). Highly anisotropic, state- and energy-dependent angular distributions emerged for all sizes. Well-defined classes of energy dependence related to the approximate angular momenta of the bound-state orbitals indicate that the overall character of the valence electron wave functions is not appreciably influenced by the interaction with the ion background. The measured distributions nevertheless deviate strongly from the predictions of single-electron models, hinting at a distinct role of correlated multielectron effects in the photoemission process.

Under the free-electron model, a cluster of metal atoms can be seen as a realization of the textbook case of a spherical box potential filled with a well-defined number of electrons, and therefore as an ideal model system to study the structure and dynamics of a finite-size Fermi system. In such a system, the electrons occupy angular momentum eigenstates, which leads to a highly discretized density of states—the electron shell structure (1, 2). By analogy with atomic orbital filling, the clusters can thus be

construed as “artificial atoms” (3). Sodium is the best representative of a free-electron metal (4), and indeed it was for sodium clusters that an influence of this shell structure was initially observed (5). This result inspired a wealth of studies on simple metal clusters, and shell effects have been found in many cluster properties, for example, in the size dependences of binding energies, ionization potentials, and absorption spectra (1). Nevertheless, photoelectron spectroscopy, which in principle allows a direct imaging of



Supporting Online Material for

Brightly Fluorescent Single-Walled Carbon Nanotubes via an Oxygen-Excluding Surfactant Organization

Sang-Yong Ju, William P. Kopcha, Fotios Papadimitrakopoulos*

*To whom correspondence should be addressed. E-mail: papadim@mail.ims.uconn.edu

Published 6 March 2009, *Science* **323**, 1319 (2009)
DOI: 10.1126/science.1166265

This PDF file includes:

Materials and Methods

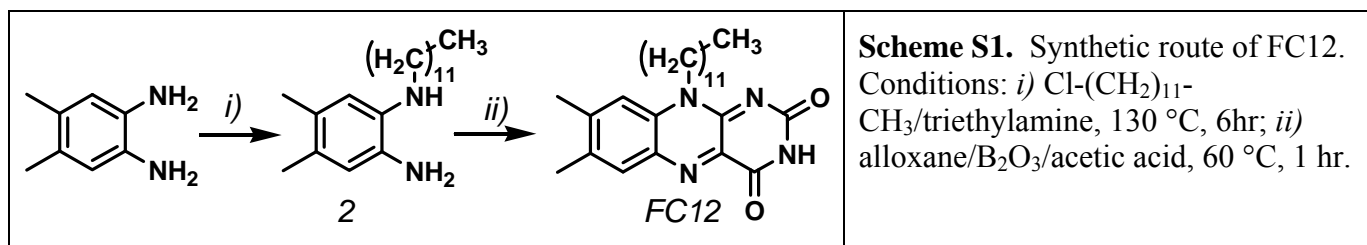
Figs. S1 to S6

Tables S1 and S2

References

Materials and Methods:

4,5-dimethyl-1,2-phenylenediamine was purchased from TCI America. 2-[*p*-dimethylaminophenyl]-2,4-neopentylene-1,3,5,7-octatetraenyl]-3-ethyl-(6,7-benzo)-benzothiazolium perchlorate (Styryl-13) was obtained from Exciton. All other reagents were purchased from Sigma-Aldrich unless otherwise mentioned. All solvents used for dispersing 10-Dodecyl-7,8-dimethyl-10*H*-benzo[*g*]pteridine-2,4-dione (FC12) and FC12-dispersed single-walled carbon nanotubes (SWNTs) were reagent grade. Synthesis of FC12 was adapted according to prior literature reports,^{1,2} and are briefly described below. Silica gel with 230-400 mesh was used for flash chromatography. Column chromatography was performed in a Companion flash chromatography apparatus (Teledyne Isco Inc.), equipped with a single wavelength UV detector. ¹H and ¹³C NMR spectra were acquired on a Bruker DMX spectrometer operating at a Larmor frequency of 400 MHz and 100 MHz, respectively. All spectra were recorded in 5 mm NMR tubes containing 0.65 ml of CDCl₃ at 295 K. SWNT prepared by the Co/Mo catalyst (CoMoCAT, lot # SG-000-0002) was kindly donated from Southwest NanoTechnologies Inc. Room temperature UV-Vis-NIR absorption spectra were obtained using a Perkin-Elmer LAMDA-900 UV-NIR spectrometer. Fluorescence spectroscopy measurements were conducted on a Jobin-Yvon Spex Fluorolog 3-211 spectrofluorometer equipped with a PMT near-infrared (NIR) detector. The intensities were corrected for instrumental variations in excitation intensity and detection sensitivity. 3 nm step size was utilized for both excitation and emission. Dynamic light scattering (DLS) was performed using NiCOMP 380/DLS submicron particle sizer equipped with a 633 nm laser (operating at a power of 5 mW), in which scattered light was collected at 90°. Prior to measurements, all samples were equilibrated at least for 10 min at 20°C to establish thermal and convectional stability.



Synthesis of FC12:

***N*-Dodecyl-4,5-dimethyl-benzene-1,2-diamine (2):** A mixture of 4.08 g (30 mmol) of 4,5-dimethyl-1,2-phenylenediamine and 2.04 g (10 mmol) of 1-chloro-dodecane in 20 mL of triethylamine was stirred at 130 °C for 6 hrs under argon. After cooling and addition of dichloromethane (100 mL), the organic solution was washed with aqueous Na₂CO₃ solution (10%, 40 mL). The aqueous layer was extracted twice with dichloromethane (MC, 2×100 mL). The combined organic extracts were dried over MgSO₄ and rotary evaporated to dryness. The thin-layer chromatography (TLC) retention factor (*R_f*) of the target compound **2** was 0.55 with MC:methanol (MeOH) (95:5). Compound **2** was purified by flash

chromatography on silica gel in MC:MeOH (95:5) to produce 1.8 g of reddish crystals (60 % yield); mp 53-54 °C; ¹H NMR (400 MHz, CDCl₃, see Figure S1) δ 6.56 (1H, s), 6.50 (1H, s), 3.20 (3H, broad s), 3.1 (2H, t, *J* = 8 Hz), 2.26 (3H, s), 2.21 (3H, s), 1.68 (2H, q, *J* = 7 Hz), 1.46 (2H, m), 1.34 (16H, s), 0.92 (3H, t, *J* = 8 Hz); ¹³C NMR (100 MHz, CDCl₃) δ 136.0, 131.8, 128.1, 125.9, 118.4, 113.93, 44.7, 31.9, 29.9, 29.69, 29.65, 29.5, 29.4; Anal. Calcd. for C₂₀H₃₆N₂ (MW=304.51): C, 78.88; H, 11.92; N, 9.20. Found: C, 78.95; H, 12.16; N, 9.32.

10-Dodecyl-7,8-dimethyl-10H-benzo[*g*]pteridine-2,4-dione (FC12): A mixture of 0.578 g (1.9 mmol) of compound **2**, 0.284 g (2 mmol) of alloxane monohydrate, 0.42 g (6 mmol) of boric oxide and 60 mL of glacial acetic acid was stirred at 60 °C for 1 hr. The resulting solution was quenched with 100 mL of water and the yellow precipitates were filtered and vacuum-dried. The *R_f* value of **FC12** by TLC was 0.85 with MC-MeOH (95:5). **FC12** was purified by flash chromatography on silica gel in MC:MeOH (95:5) to produce 0.46 g of yellow crystals (58 % yield); mp 223-224 °C; ¹H NMR (400 MHz, CDCl₃, see Figure S1) δ 8.85 (1H, s), 8.08 (1H, s), 7.41 (1H, s), 4.71 (2H, broad t), 2.59 (3H, s), 2.48 (3H, s), 1.88 (2H, q, *J* = 8 Hz), 1.57 (2H, q, *J* = 8 Hz), 1.51 (2H, m), 1.29 (14H, s), 0.90 (3H, t, *J* = 8 Hz); ¹³C NMR (100 MHz, CDCl₃) δ 159.6, 155.2, 148.2, 137.0, 136.2, 135.0, 132.9, 131.1, 115.3, 45.36, 31.9, 29.61, 29.59, 29.54, 29.50, 29.32, 29.29, 27.16, 26.9, 22.7, 21.7, 19.5, 14.1; λ_{max} (ε) 443 nm (11,964 L/mol-cm in ethyl acetate); Anal. Calcd. for C₂₄H₃₄N₄O₂ (MW=410.55): C, 70.21; H, 8.35; N, 13.65; O, 7.79. Found: C, 70.09; H, 8.85; N, 13.41.

Nanotube Dispersion Protocols:

Dispersion of FC12/SWNT in organic solvents: A mixture of 1 mg of CoMoCAT-SWNT and 1 mg (2.4 μmol) of FC12 in 4 mL of organic solvents were cup-horn sonicated for 4 hrs at 300 W (Cole Parmer Ultrasonic Processor). All resulting solutions were centrifuged at 10,000 g for 20 min followed by careful collection of their supernatants, unless otherwise noted.

Dispersion of SDS/SWNT in D₂O: A mixture of 1 mg of CoMoCAT-SWNT and 1 wt. % of SDBS was added into 4 mL of D₂O, according to literature.³ The solution was homogenized for 1 hr, followed by sonication for 10 min at 600W intensity. The resulting solution was centrifuged at 45,000 g for 2 hr and the supernatant (upper 80 %) was collected to produce a clear dark solution.

Dispersion of FMN/SWNT in D₂O: A mixture of 1 mg of CoMoCAT-SWNT and 4 mg of FMN in 4 mL of D₂O were cup-horn sonicated for 4 hrs at 300 W (Cole Parmer Ultrasonic Processor), as detailed elsewhere.⁴ The solution were centrifuged at 15,000 g for 2 hrs followed by careful collection of their supernatants.

Protocols for the Deconvolution of Vis-NIR Absorption Spectra:

Background corrections for Fig. 3b&c were carried out by subtracting a power-law function ($a\lambda^{-b}$, where λ is the wavelength and a , b are fitted parameters), as described elsewhere.⁵ The b value was obtained from an optimum fit of the background signal. The optimum values of b for toluene, ethyl acetate and acetone dispersion in Fig. 3b&c were found to be 0.600, 0.815, and 0.671, respectively. Peak deconvolution using Lorentzian peak profiles were found to produce an optimum fit for the toluene sample of Fig. 3b. In the case of ethyl acetate and acetone samples, deconvolution of their NIR absorption spectra was performed using Voigt peak profiles.

Photoluminescence (PL) Quantum Yield (QY) Measurements:

PL QY was calculated using Styryl-13 (2-[*p*-dimethylaminophenyl]-2,4-neopentylene-1,3,5,7-octatetraenyl]-3-ethyl-(6,7-benzo)-benzothiazolium perchlorate) as a reference dye, with 11 % reported QY (η_{ref}) according to Crochet *et al.*⁶ The sample QY (η_s) was determined based on equation (1),

$$\eta_s = \eta_{ref} \times \frac{I_s \times \alpha_{ref} \times n_s^2}{I_{ref} \times \alpha_s \times n_{ref}^2} \quad (1)$$

Where I is the integrated area of photoluminescence emission, α is the extinction coefficient at the excitation wavelength, and n is the refractive index of the solvent, for the sample (s) and reference (ref), respectively. The extinction coefficient α was obtained from the respective peak height of the absorption band at the excitation wavelength. The concentration of all samples was adjusted to similar absorption values (*i.e.* less than 0.05) at 580 nm. The emission spectra of Styryl-13 (in methanol), FC12/SWNTs (in toluene), and SDS/SWNTs (in D₂O) were recorded at 580, 583, and 569 nm, excitation wavelengths, using the same slit widths for the mercury lamp as well as the excitation and emission monochrometers. In order to determine the concentration dependence of PL QY of SDS-dispersed SWNTs, a stock SDS/SWNTs D₂O dispersion was diluted with 1% w/v SDS dispersion in D₂O to maintain the similar SDS concentration throughout the experiment.

Molecular Modeling:

Cerius2 simulation software was utilized for molecular modeling using the Dreiding 2.21 force field for molecular mechanics, molecular dynamics and quenched dynamics simulations, as detailed elsewhere.⁴ The charge equilibration method was used to set atom charges for 10-methyl isoalloxazine (lumiflavin), while zero charge was assigned for all SWNT carbon atoms. Materials Studio 4 software was used for visualization. An sp^3 geometry was used for the N atom at the 10 position of the isoalloxazine ring (Scheme S1), while for the rest of the aromatic atoms an sp^2 configuration was utilized. For the general approach, various helix motives U_i were constructed using symmetry operation, where U and t denote

number of helical lattice points per identical period and turns to the next identical helix point, respectively. A vertically-aligned flavin moiety was off-centered by the summated distance of half of diameter of SWNT (*i.e.*, 0.38 nm for (6,5) nanotube) and van der Waals distance (0.34 nm). This flavin moiety was then rotated by $(360^\circ \times t)/U$ and translated by $(2.5 \text{ nm} \times t)/U$ along z-axis, which is parallel to SWNT axis. The resulting half helix was rotated along the x-axis and adjusted to generate a complementary double helix. The combined double stranded flavin helix was minimized in the periodic boundary condition, while energy-minimization to the underlying carbon nanotube was constrained. For energy-minimization of nanotube with various U_i flavin helices in periodic boundary condition, the iteration was repeated until RMS values are below 0.001 kcal/mol/atom. For the 1,4-endoperoxide defects onto SWNT (Fig. 1C), the energy-minimized configuration was found close to the reported DFT conformation.⁷ A purple shading was added to the 1,4-endoperoxide of Fig. 1C to better visualize the radii of space-filled oxygen atoms.

Figure S1. ^1H NMR spectra of compound **2** and FC12. Green and black stars indicate peaks from CDCl_3 and residual water.

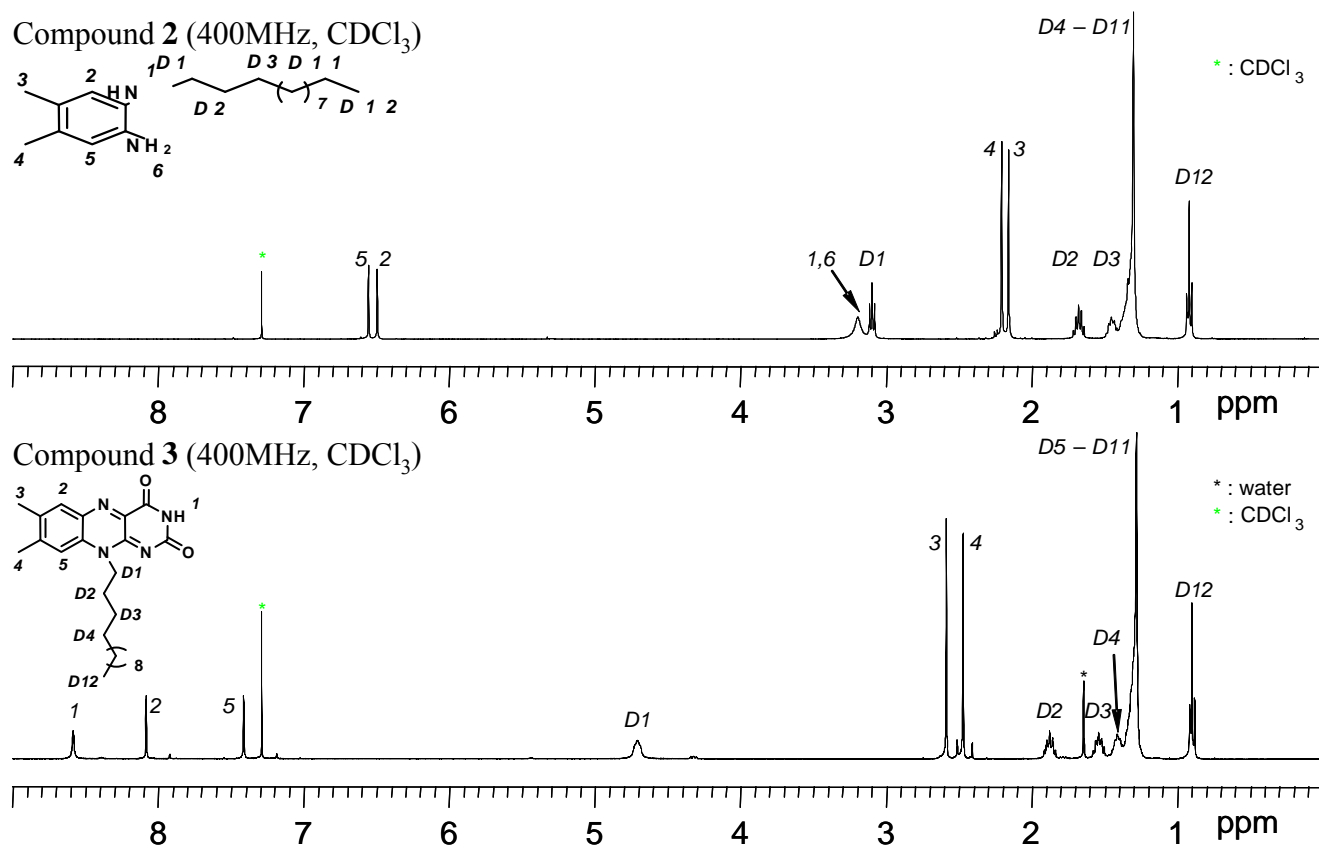


Figure S2. Relative PL intensity of FC12/SWNTs in various solvents, plotted as a function of nanotube diameter. Relative PL intensity of SDS/SWNTs was also presented. All peak intensities are listed in Table S2 and the total sum is 100%.

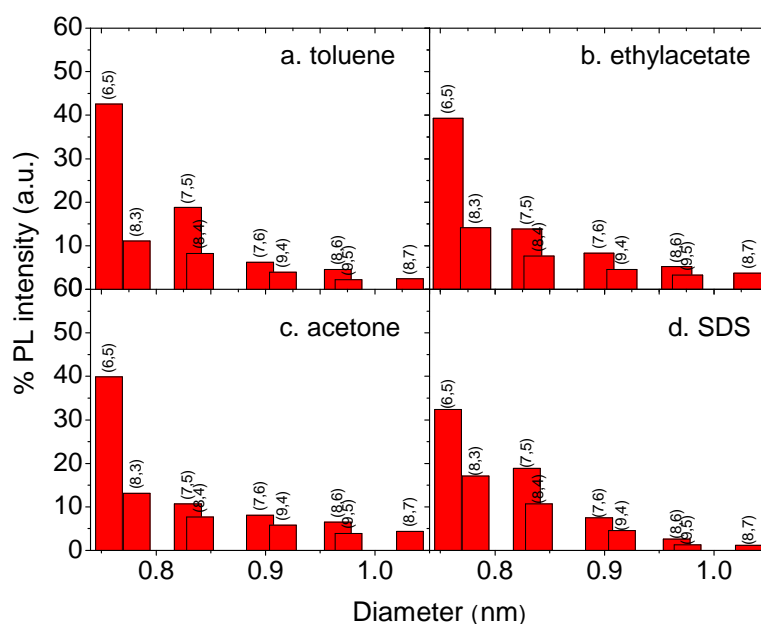


Figure S3. Excitation slices at 1047 nm emission from Fig. 2a-d.

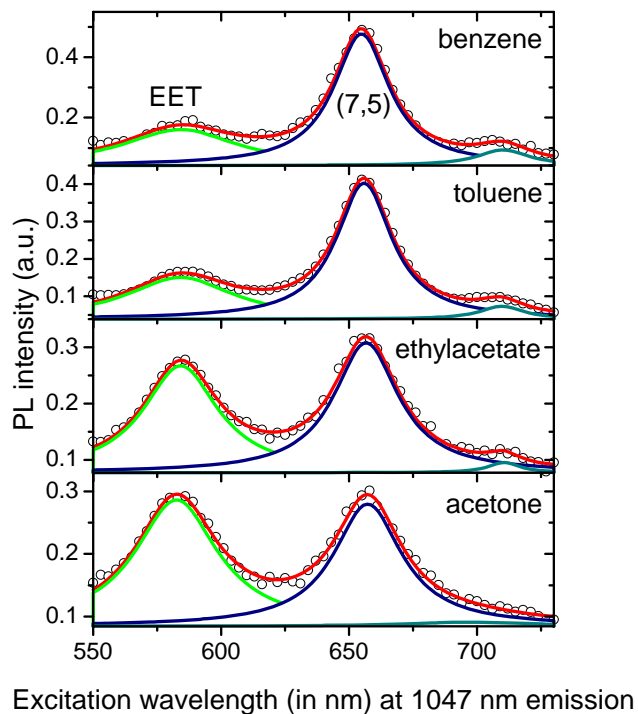


Figure S4. Absorption spectra close-up from ethyl acetate (a) and acetone (b), along with their deconvoluted components in the absence of the orange-colored Gaussian peak contribution shown in Fig. 3c (top two spectra). Red curve shows the summated absorption spectra from the color-coded individual fitting curves, while circled curves depict the background subtracted, experimentally obtained absorption spectra.

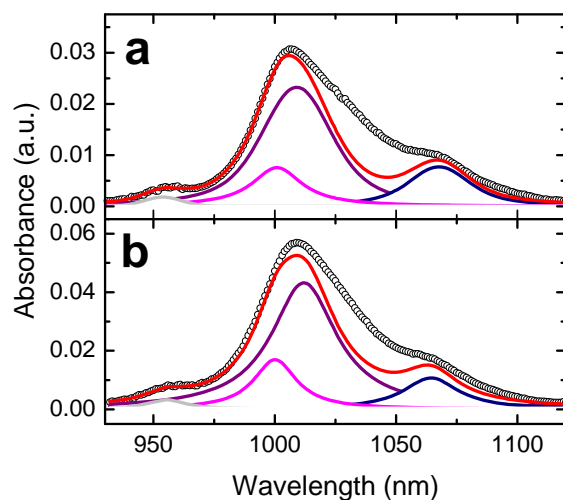


Figure S5. Auto-correlation function ($C(t)$) of dynamic light scattering (DLS) of FC12/SWNTs dispersed in toluene (black) and ethylacetate (red).

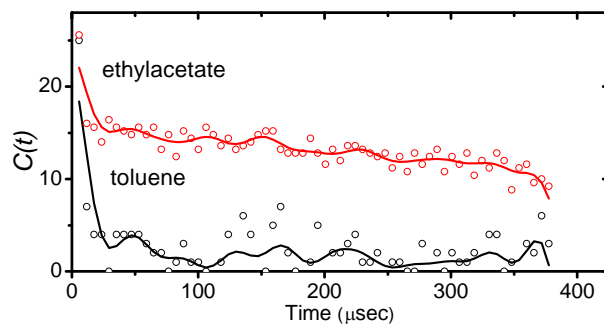


Figure S6. (6,5)-SWNT “sample” photoluminescence (PL) quantum yields (QYs) for SDS-dispersed nanotubes in D_2O as a function of its E_{22}^S absorption peak intensity. Inset illustrates the SDS-dispersed (6,5)-SWNT PL peak area change as a function of its E_{22}^S absorption peak intensity.

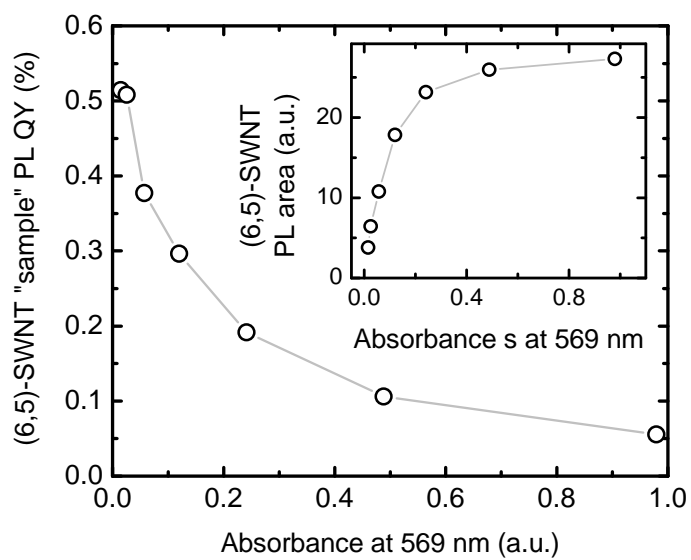


Table S1. PLE-derived E_{11}^S and E_{22}^S positions and relative PL intensities from Figure 2a-d.

Nanotube Assignment	Diameter	Chiral Angle	Benzene				Toluene				Ethyl acetate				Acetone			
			E_{11}^S	E_{22}^S	FWHM _{E11}	Rel. Int.	E_{11}^S	E_{22}^S	FWHM _{E11}	Rel. Int.	E_{11}^S	E_{22}^S	FWHM _{E11}	Rel. Int.	E_{11}^S	E_{22}^S	FWHM _{E11}	Rel. Int.
	nm	degree	nm	nm	meV		nm	nm	meV		nm	nm	meV		nm	nm	meV	
(9,1)	0.757	5.21					945.1	707.0	24.99									
(6,5)	0.757	27.00	992.1	582.2	32.69	1.000	993.8	582.8	33.70	1.000	998.7	582.4	39.31	1.000	998.8	582.5	41.50	1.000
(8,3)	0.782	15.30	980.8	673.8	21.89	0.253	982.0	674.8	20.70	0.236	987.8	674.0	34.28	0.381	989.3	674.2	31.36	0.352
(7,5)	0.829	24.50	1049.0	654.8	29.69	0.490	1048.6	655.9	29.58	0.411	1056.4	654.7	35.87	0.363	1052.7	658.9	55.13	0.296
(8,4)	0.840	19.11	1123.4	603.0	29.25	0.158	1125.7	603.2	29.00	0.173	1139.8	606.9	42.07	0.205	1143.9	607.9	51.38	0.176
(7,6)	0.895	27.46	1153.7	658.3	21.34	0.120	1152.2	659.5	30.70	0.165	1147.2	658.9	42.51	0.193	1154.3	659.1	51.34	0.184
(9,4)	0.916	17.48	1122.5	740	29.99	0.074	1122.5	740.1	29.00	0.081	1131.1	735.3	44.35	0.126	1136.0	741.3	51.80	0.118
(8,6)	0.966	25.28	1202.9	737	25.70	0.102	1204.6	737.8	23.23	0.091	1207.9	736.2	30.16	0.139	1216.8	735.3	37.48	0.167
(9,5)	0.976	20.63	1272.7	691.6	20.67	0.051	1272.2	691.6	24.05	0.094	1275.8	687.8	38.36	0.081	1279.2	688.0	39.79	0.092
(8,7)	1.032	27.80	1308.0	744.1	22.91	0.075	1308.0	744.1	22.91	0.049	1308.5	743.0	47.36	0.099	1311.7	745.7	45.05	0.126

Table S2. (n,m) abundance evaluation of FC12/SWNTs in toluene as determined from their Vis-NIR absorption (Fig. 3b) and PLE map (Fig. 2b and Table S1), listed for increasing nanotube diameter (d_t).

Assign. (n,m)	d_t (nm)	FWHM (meV)	Abs _{measured} (%)	PL _{measured} Intensity (%)	Divergence [‡]	Abs scaling factor [§]	PL scaling factor [§]	Scaled Abs (%)	Scaled PL (%)	Divergence [‡]	
(9,1)	0.76	15.8	1.8	0.5	0.28	2.75	0.70	1.3	0.4	0.26	
(6,5)	0.76	24.6	50.1	42.4	0.04	1.85	0.67	52.7	40.4	0.07	
(8,3)	0.78	15.1	4.2	11.0	0.22	2.43	2.13	3.3	3.3	0.00	
(7,5)	0.83	18.7	8.6	18.7	0.18	2.04	0.71	8.2	16.8	0.17	
(8,4)	0.84	19.4	3.8	8.2	0.18	1.77	0.46	4.2	11.4	0.23	
(7,6)	0.90	30	11.3	6.2	0.15	1.98	0.47	11.1	8.4	0.07	
(9,4)	0.92	12.1	1.2	3.8	0.26	2.27	0.70	1.1	3.5	0.26	
(8,6)	0.97	16.8	5.5	4.6	0.04	2.18	0.49	4.9	6.0	0.05	
(9,5)	0.98	18.6	6.0	2.2	0.23	1.88	0.28	6.3	5.1	0.05	
(8,7)	1.03	21.7	7.4	2.4	0.26	2.06	0.30	7.0	5.2	0.07	
Average divergence [‡] value before scaling					0.18	Average divergence [‡] value after scaling					0.12

[‡] Divergence: $0.5 \times | \% \text{Abs} - \% \text{PL} | / (\% \text{Abs} + \% \text{PL})$

[§] according to Oyama *et al.*⁸

Cited References

1. Ju, S. Y.; Papadimitrakopoulos, F. *J. Am. Chem. Soc.* 2008, 130, (2), 655-664.
2. Nakade, H.; Jordan, B. J.; Xu, H.; Han, G.; Srivastava, S.; Arvizo, R. R.; Cooke, G.; Rotello, V. M. *J. Am. Chem. Soc.* 2006, 128, (46), 14924-14929.
3. O'Connell, M. J.; Bachilo, S. M.; Huffman, C. B.; Moore, V. C.; Strano, M. S.; Haroz, E. H.; Rialon, K. L.; Boul, P. J.; Noon, W. H.; Kittrell, C.; Ma, J.; Hauge, R. H.; Weisman, R. B.; Smalley, R. E. *Science* 2002, 297, (5581), 593-596.
4. Ju, S.-Y.; Doll, J.; Sharma, I.; Papadimitrakopoulos, F. *Nat. Nanotech.* 2008, 3, 356-362.
5. Luo, Z.; Pfefferle Lisa, D.; Haller Gary, L.; Papadimitrakopoulos, F. *J. Am. Chem. Soc.* 2006, 128, (48), 15511-15516.
6. Crochet, J.; Clemens, M.; Hertel, T. *J. Am. Chem. Soc.* 2007, 129, (26), 8058-8059.
7. Dukovic, G.; White, B. E.; Zhou, Z.; Wang, F.; Jockusch, S.; Steigerwald, M. L.; Heinz, T. F.; Friesner, R. A.; Turro, N. J.; Brus, L. E. *J. Am. Chem. Soc.* 2004, 126, (46), 15269-15276.
8. Oyama, Y.; Saito, R.; Sato, K.; Jiang, J.; Samsonidze, G. G.; Gruneis, A.; Miyauchi, Y.; Maruyama, S.; Jorio, A.; Dresselhaus, G.; Dresselhaus, M. S. *Carbon* 2006, 44, (5), 873-879.